Journal of Materials Chemistry A

ROYAL SOCIETY OF CHEMISTRY

PAPER

Cite this: J. Mater. Chem. A, 2024, 12, 30831

Achieving dynamic stability of single-crystal low-Co Ni-rich cathode material for high performance lithium batteries†

Adil Saleem,[a] Leon L. Shaw, *[a] Mehwish Khalid Butt,[b] Javed Rehman,[b] Arshad Hussain,[c] Zawar Hussain,[d] Rashid Iqbal*[e] and Muhammad Kashif Majeed*[f]

Received 7th July 2024
Accepted 14th October 2024

DOI: 10.1039/d4ta04698f

rsc.li/materials-a

The demand for high-energy-density lithium-ion batteries (LIBs) has driven intensive research into cathode materials that exhibit both superior performance and stability over multiple charge–discharge cycles. This work focuses on enhancing the dynamic stability of single-crystal (SC) low-cobalt (Co) nickel-rich (Ni-rich) cathode materials, crucial for the advancement of LIB technology. The proposed strategy involves co-doping of iron (Fe) and aluminum (Al) with an optimized composition to mitigate the capacity degradation and voltage fading observed for traditional Ni-rich (≥90%) cathodes. Through a comprehensive investigation combining theoretical modeling, material synthesis, and electrochemical characterization, the synergistic effects of Fe/Al co-doping are elucidated. The presence of Fe and Al ions in the crystal lattice not only stabilizes the structural integrity but also facilitates the suppression of phase transformation and surface degradation during cycling. Moreover, the incorporation of Fe and Al ions optimizes the lithium (Li)-ion diffusion kinetics and enhances the electronic conductivity, leading to improved electrochemical performance. The achieved dynamic stability of the co-doped SC cathode material enables prolonged cycle life and high-rate capability, making it a promising candidate for next-generation LIBs.

1. Introduction

The mission for more efficient and reliable energy storage solutions has led to intensive research and development in the field of LIBs.[1–3] Among the key components of LIBs, cathode materials play a crucial role in determining the battery's performance and durability.[4,5] In recent years, there has been a growing interest in exploring Ni-rich cathode materials due to their high energy density and potential for reducing reliance on expensive and scarce Co.[6–8] However, challenges such as stability during cycling have emerged, prompting researchers to delve into innovative approaches to enhance the performance of Ni-rich cathodes.[4,9,10] In response, it is imperative for the sustainable advancement of LIBs to completely eliminate Co from the current cathode material composition.[11] However, Co-free cathodes often exhibit significant structural deficiencies, such as the occurrence of Li/Ni cation mixing, leading to diminished capacity and sluggish Li-ion diffusion due to magnetic frustration effects.[12–14] Additionally, the thermal breakdown of Co-free cathodes during charging can lead to uncontrollably high temperatures, triggering exothermic reactions between the electrolyte and liberated oxygen, posing a potential risk of thermal runaway and serious safety concerns.[15] Enormous efforts have been invested in determining the causes of the inferior failure mechanism.[16–21] Consequently, the pursuit of Co-free cathodes with both practical capacity and stability suitable for industrial applications remains an exceptionally challenging endeavor.

Indeed, adopting a SC design presents a pragmatic approach to mitigating the challenges associated with low-Co Ni-rich cathodes, particularly in bolstering their thermal stability and longevity across cycling.[22–25] These materials exhibit unique structural and electrochemical properties that can significantly impact battery performance. In addition, SC structures can minimize the structural defects and grain boundaries, which are known to contribute to performance degradation and reduced stability in traditional polycrystalline cathodes.[26] The dynamic stability of these SC low-Co Ni-rich cathode materials

[a]Department of Mechanical, Materials and Aerospace Engineering, Illinois Institute of Technology, Chicago, IL, USA. E-mail: lshaw2@iit.edu

[b]State Key Laboratory of Metastable Materials Science and Technology, and School of Materials Science and Engineering, Yanshan University, Qinhuangdao 066004, China

[c]Interdisciplinary Research Center for Hydrogen and Energy Storage, King Fahd University of Petroleum & Minerals, Dhahran 31261, Saudia Arabia

[d]Institute for Advanced Study, Shenzhen University, Shenzhen 518060, China

[e]Key Laboratory of Colloid and Interface Chemistry of the Ministry of Education, School of Chemistry and Chemical Engineering, Shandong University, 250100 Jinan, China. E-mail: rashid@szu.com

[f]Department of Mechanical Engineering, The University of Texas at Dallas, Richardson, TX, USA. E-mail: drmkm@utdallas.edu

† Electronic supplementary information (ESI) available. See DOI: https://doi.org/10.1039/d4ta04698f

refers to their ability to maintain structural integrity and electrochemical performance over numerous charge–discharge cycles.[27,28] Achieving dynamic stability is crucial for extending the lifespan and enhancing the reliability of LIBs, especially in demanding applications such as electric vehicles and grid storage.

Recently, incorporating different cations, such as Mg^{2+}, Al^{3+}, Fe^{3+}, and Ti^{4+}, into the layered structure has proven effective in enhancing structural stability, surface oxygen retention, and thermal stability.[22,23,29,30] Additionally, the inclusion of cations with larger radii, such as Zr^{4+} and W^{5+}, during $LiNiO_2$ synthesis has led to the preferential segregation of a secondary phase onto primary particle surfaces.[23,31] This parasitic secondary phase acts as a physical barrier, effectively isolating the parent phase from the electrolyte and thereby inhibiting interfacial side reactions. An increasing number of studies have explored the application of multiple dopants in layered oxides, aiming to leverage synergistic effects that enhance the individual roles of each dopant.[32,33] The ongoing exploration of dopant combinations underscores the dynamic and evolving nature of materials science in optimizing battery performance for future applications.[34–36] One strategy involves precise control over the synthesis parameters to tailor the crystal structure and optimize the electrochemical properties of the cathode material. By minimizing Co-content and engineering the Ni-rich phase the stability and cyclability of the cathode material can be significantly improved.[37]

Herein, we propose Fe/Al co-doped SC $LiNi_{0.90}Mn_{0.05}Fe_{0.02}Al_{0.02}Co_{0.01}O_2$ (NMFAC) cathode material with low-Co content, benchmarked against the pristine SC $LiNi_{0.90}Mn_{0.05}Co_{0.05}O_2$ (NMC) cathode synthesized through coprecipitation followed by molten flux method. The high Ni-content is essential for providing a high capacity, however, adding a small amount of Fe^{3+} (0.55 Å) and Al^{3+} (0.54 Å), with almost similar ionic radii as Ni^{3+} (0.56 Å), could replace some of the Ni and improve cycle life, structural stability, and safety.[38,39] The co-presence of Mn and Al in Ni-rich cathodes is critical to thermal and cycle stability, which efficiently inhibit the multistep phase transitions of $LiNiO_2$ during delithiation.[40,41] Besides, Mn tends to increase Li/Ni cation mixing, whereas Al tends to decrease it; Al is good at moderating transition-metal (TM) dissolution, while Mn appears to have no such advantages.[42] Meanwhile, Al usage is often restricted to ≤5–6 mol% to prevent secondary phases, while Mn can be added up to 33–50 mol% in Ni-based layered oxides without structural reconstruction into a spinel phase.[43,44] The introduction of Al into the host layered structure stabilizes the crystal structure, resulting in Ni-rich cathodes with high capacity and long cycle life, outperforming conventional cathodes with the same Ni content.[34] Fe^{3+} dopant has a similar electronic structure and the same oxidation state as Co^{3+}, which helps minimize Li/Ni cation mixing by lowering the interlayer linear Ni^{2+}–O^{2-}–Fe^{3+} super-exchange interactions.[45] Substituting Fe^{3+} for TM ions in SC NMC helps to create a high entropy oxide layer and strong TM–O–Fe bonds. This effectively suppresses oxidation and the migration of lattice oxygen due to the electrochemical inactivity of Fe^{3+} ions.[46] Co-doping of Fe and Al is expected to offer synergistic effects of combining the advantages of both elements, leading to (i) reductions in capacity degradation and voltage fading by preventing the layered-to-spinel phase transition, avoiding the migration of Ni ions into the Li layer and minimizing the lattice oxygen release, and (ii) added thermal stability and reduced surface reactivity to minimize electrolyte decomposition and related side reactions. Such expectations are demonstrated in this study. On the interphase front, time-of-flight secondary ion mass spectrometry (TOF-SIMS) is utilized to see and quantitatively analyze the cathode–electrolyte interphase (CEI). In conclusion, we clarify the advantages of a low-Co Ni-rich cathode and determine that the NMC cathode chemistries can be substituted with the combination of Fe and Al. These findings emphasize the probability of the co-doping strategy and demonstrate the NMFAC viability for real-world use in inexpensive LIB systems.

2. Experimental section

2.1 Materials preparation

The hydroxide precursors of NMFAC and NMC ($Ni_{0.90}Mn_{0.05}Fe_{0.02}Al_{0.02}Co_{0.01}(OH)_2$ and $Ni_{0.90}Mn_{0.05}Co_{0.05}(OH)_2$, respectively) were synthesized *via* coprecipitation. Aqueous solutions containing $NiSO_4 \cdot 6H_2O$, $FeSO_4 \cdot 7H_2O$, $Al_2(SO_4)_3 \cdot H_2O$, $MnSO_4 \cdot 5H_2O$, and $CoSO_4 \cdot 7H_2O$ at concentrations of 2.0 M and their respective stoichiometric ratios were prepared in deionized water. Solutions of 4.0 M $NH_3 \cdot H_2O$ and 5 M NaOH were also prepared separately. These solutions were simultaneously transferred into a stirred tank reactor with controlled conditions of temperature (55 °C), pH (11.5), and stirring speed (650 rpm) during the coprecipitation process. The resulting hydroxide precursors were subsequently washed with deionized water, filtered, sieved, and dried at 100 °C overnight to remove excessive water. The obtained hydroxide powder then underwent calcination at 900 °C for 15 hours in oxygen atmosphere to obtain oxide precursor ($Ni_{0.90}Mn_{0.05}Fe_{0.02}Al_{0.02}Co_{0.01}O_2$ and $Ni_{0.90}Mn_{0.05}Co_{0.05}O_2$). The resulting oxide precursors were then mixed with lithium oxide at a molar ratio of 1 : 0.8, followed by the addition of NaCl (at a 1 : 1.1 weight ratio). Here, NaCl with a melting point of 801 °C was used as a molten salt medium to lower the reaction temperature and time for growth of single crystals (SC). The oxide precursor + LiH + NaCl mixture was homogenized and well ground, and then heated at 800 °C for 10 hours, followed by 900 °C for 5 hours in oxygen atmosphere. The final products were washed with ethanol to remove the residual impurities from the samples after the molten salt process and dried in vacuum at 80 °C for 2 hours. Following this, post annealing was performed at 580 °C for 4 hours in an oxygen atmosphere before the end products were collected. Fig. 1 schematically illustrate the synthesis procedure for both NMC and NMFAC.

2.2 Electrochemical testing

Cathode active material with poly(vinylidene fluoride) (PVDF) and conductive carbon (Super P) with weight ratios 90 : 5 : 5 in *N*-methyl-2-pyrrolidone (NMP) solvent were used to prepare cathode slurries. The as-prepared slurries were casted on Al foil

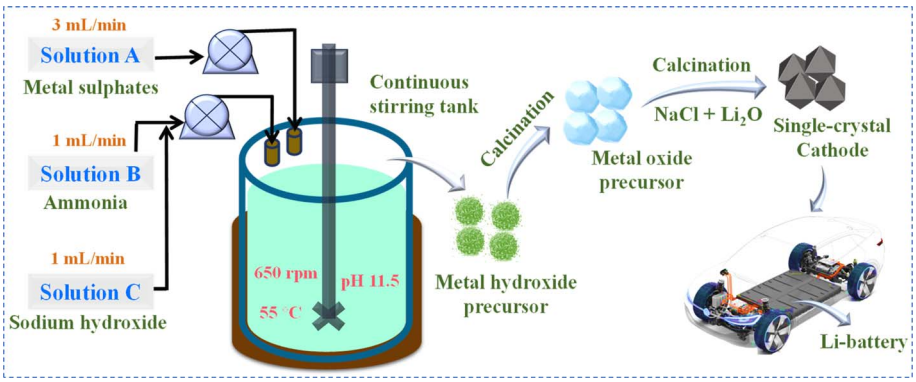

Fig. 1 Schematic illustration of the synthesis process for NMC and NMFAC.

with ~2.2 to 2.4 mA h cm^{-2} active material loadings and dried overnight in a 90 °C vacuum oven. After undergoing drying, calendaring, and punching, the electrodes were utilized as cathodes in both coin half-cell and full-cell tests. For the full cells, a mixture of graphite, conductive carbon and PVDF binder in NMP (mass ratio: 90 : 2.5 : 7.5) was prepared as the anode. This anode slurry was coated onto a copper foil with a graphite loading of approximately 2.3–2.4 mA h cm^{-2}. The electrolyte used in this work contained 1 M $LiPF_6$ in a blend of ethylene carbonate, ethyl methyl carbonate, and dimethyl carbonate (EC/EMC/DMC, 1 : 1 : 1 by weight) containing 2 wt% vinyl carbonates (VC) as an additive. The electrochemical performance of the fabricated coin half-cell and full-cell was evaluated using a battery testing system (LAND CT2001A, China) across various current rates within a voltage range of 2.8–4.3 V at room temperature.

2.3 Materials characterization

Powder X-ray diffraction patterns were collected by Rigaku Miniflex 600 X-ray diffractometer with Cu Kα radiation (λ = 1.54184 Å). The surface morphologies were examined by a scanning electron microscope (SEM; JSM-7800F) and transmission electron microscope (TEM; JEOL F200) equipped with energy dispersive X-ray spectroscopy (EDX) to examine the particle shape and elemental distribution. The cathode's chemical composition was analyzed using an inductively coupled plasma optical emission spectrometer (ICP-OES; ICAP 7000). X-ray photoelectron spectroscopy (XPS; Ulvac-PHI 5000) was employed to investigate the chemical state of the main elements present on the surface of the active materials. The cathode–electrolyte interphase characterization was carried out with time-of-flight secondary ion mass spectroscopy (PHI nano TOF-SIMS) with a mass resolution of 30 keV energy and Bi_3^{++} ion analysis beam (sputtering areas 100 × 100 μm^2).

2.4 Computational methodology

All the calculations in this work have employed density functional theory (DFT), utilizing the plane-wave method executed in the Vienna *ab initio* simulation package (VASP). The projected augmented wave (PAW) method displayed the correlations between ions and electrons. A cut-off energy of 550 eV was taken with a plane-wave basis, and exchange–correlation energy was modeled using the Perdew, Burke, and Ernzerhof (PBE) functional. The convergence criteria for the geometry optimization were set to be 10^{-6} eV for energy and 10^{-2} eV $Å^{-1}$ for Hellmann–Feynman force. A 2 × 2 × 1 supercell with a Monkhorst Pack special *k*-point mesh of 3 × 3 × 3 was taken for Brillouin zone integration. For Ni, Mn, Fe, Al, and Co, DFT + U parameters of 6.8, 5.2, 4.9, 5.2, and 3.4 eV were used.

3. Results and discussion

Theoretical and computational methodologies, particularly DFT, represent a promising avenue for digging into the behaviors of material defects and establishing correlations between structure and properties.[47] Fig. 2a illustrates the optimized atomic structure of the lowest energy configuration of the NMFAC cathode, revealing a preference for Fe/Al substitution at the Ni-site and the stability of a layered crystal structure, consistent with prior research findings[48,49] as well as the XRD analysis of this study (to be discussed later). Furthermore, the close agreement in the lattice parameters between the experimental results derived from the XRD analysis (Table S1†) and DFT calculation demonstrates the accuracy of the DFT approach in predicting structural changes due to Fe/Al co-doping. Analysis of the density of states (DOS) and partial density of states (PDOS) in proximity to the Fermi level predominantly showcases highly redox-active Ni^{3+} states (3d-states). It can be observed that NMFAC cathode is half metals, and these computations suggest that the conductivity of NMFAC cathode is comparable to NMC (Fig. 2b–d).[50,51] Due to the similar energy level and conductivity, it is additionally verified that the innovative low-Co cathode material demonstrates a Li^+ diffusion rate equivalent to that of the traditional NMC cathode. Fig. 2e and Table S2† show the impact of Fe/Al doping on the transition metal ion–oxygen bonds. This analysis underscores that the longer bond length of Fe–O shows superior oxygen stability at high delithiation as compared to Co by Mn–Fe.[52] Note that Fe–O links are heavily hybridized into metal–oxygen bonds as indicated by the comparable energy states between the Fe d-band and the O p-band, which readily

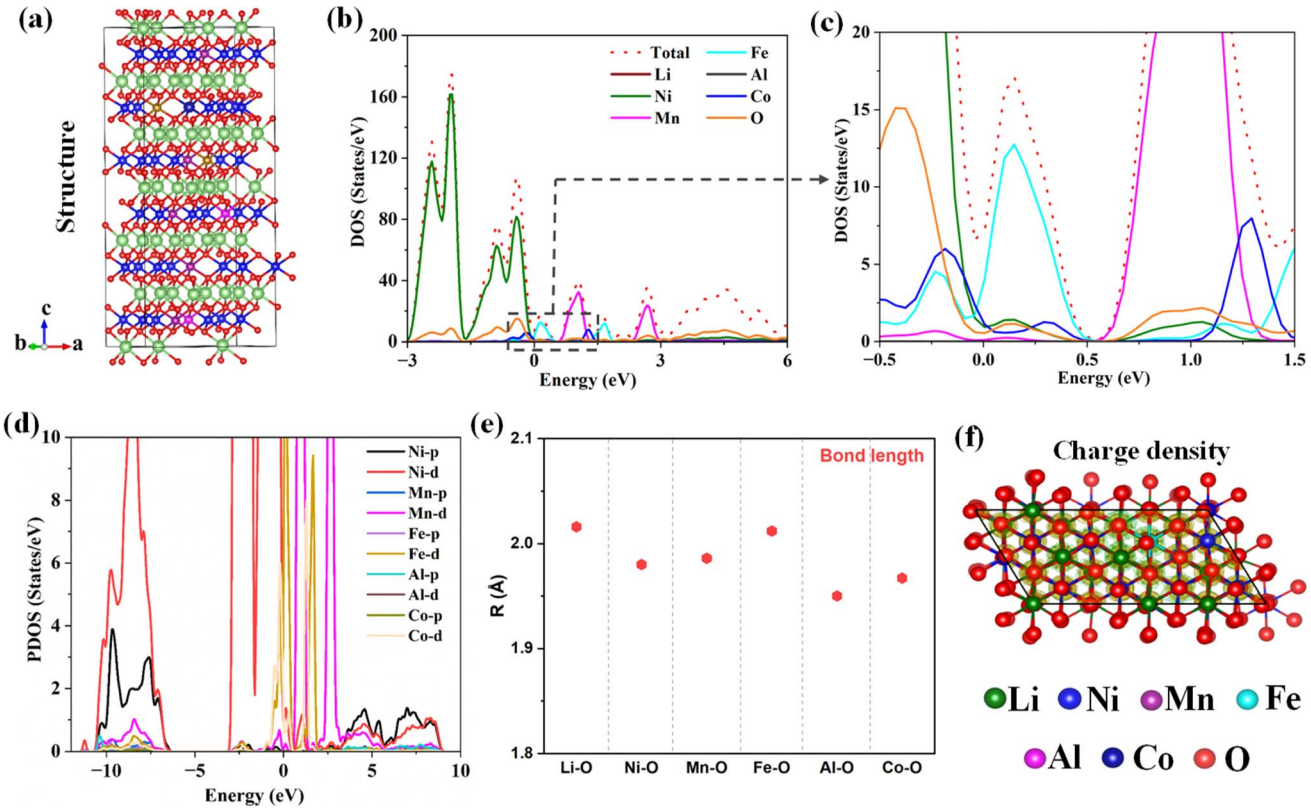

Fig. 2 (a) Optimized atomic structure of NMFAC cathode. (b–d) Calculated density of states and partial density of states for NMFAC. (e and f) Bond length and charge density distribution for NMFAC.

cause oxygen instability during charging. However, partial Mn substitution for Co can reduce oxygen instability because Mn has a greater energy difference *versus* the oxygen p-band.[53] When combined, NMFAC can increase safety performance by lowering the reactivity between the charged cathode and electrolyte at high temperatures. Such observations align with anticipated outcomes based on standard bond dissociation energies with oxygen. The presence of robust Fe–O bonds energy (409 kJ mol^{-1}) *vs.* Ni–O bond energy (391 kJ mol^{-1}) in NMFAC holds potential for enhancing material stability by mitigating oxygen release or phase transitions. The atomic charge density difference suggests that NMFAC exhibits less electron accumulation implying a preference for a more uniform surface capping by atoms (Fig. 2f). Superexchange metals primarily influence the alteration of Ni/Li disordering during transitions, elucidating why the exchange of Ni^{3+} in Ni-rich materials is more facile compared to Ni^{2+}.[45,54]

The XPS analysis were carried out to investigate the valence states of the metal elements in NMC and NMFAC. Fig. 3a shows the Ni 2p spectra for both NMC and NMFAC, exhibit Ni 2p3/2 and Ni 2p1/2 at ~854.9 and ~872.7 eV, respectively, corresponding to Ni^{2+}, along with a satellite peak at ~855.6 eV corresponding to Ni^{3+}. The higher proportion Ni^{2+} ions migrate to the Li layer, increasing the level of cation mixing. The partial substitution of Co^{3+} with Fe^{3+} and Mn^{4+} with Al^{3+} leading to the conversion of Ni^{2+} ions to Ni^{3+} to maintain charge neutrality and helps to overcome the drawback of increased cation mixing. The Mn 2p spectra reveals two peaks of Mn $2p_{3/2}$ and Mn $2p_{1/2}$, corresponding to Mn^{4+} and Mn^{3+}, located at ~642.03 and ~653.83 eV, respectively (Fig. 3b) with two satellite peaks at ~637.58 and ~644.08 eV. The Co 2p spectra display two peaks of Co $2p_{3/2}$ and Co $2p_{1/2}$, corresponding to Co^{3+}, located at ~780.03 eV and ~795.38 eV, respectively (Fig. 3c). However, the peaks intensity was lower for NMFAC than that of NMC. The Fe 2p spectra (Fig. 3d) for NMFAC display Fe $2p_{3/2}$ and Fe $2p_{1/2}$ located at ~711.43 and ~724.03 eV, respectively, with satellite peaks at around ~704.9, ~713.08 and ~733.38 eV, confirming the presence of Fe^{3+} state. In the Al 2p spectra for NMFAC, peaks corresponding to Al 2p3/2 and Al 2p1/2 are detected at ~67.18 and ~72.43 eV, respectively, with a satellite peak at ~68.38 eV (Fig. 3e). The less prominent XPS spectra of Al 2p and Co 2p may be attributed to their lower content in NMFAC. Additionally, the XPS survey spectrum for both NMC and NMFAC cathode materials confirms the presence of all elements, including Ni, Co, Mn, Fe, and Al (Fig. S1c and d†).

XRD was performed to analyze the structural changes in NMC cathode with Fe/Al co-doping. The XRD patterns in Fig. 3f confirmed the formation of layered structure hexagonal α-$NaFeO_2$ ($\bar{R}3m$ space group), with a clear splitting of (108)/(110) and (006)/(102) peaks in both NMFAC and NMC, indicating the high crystallinity and higher ordered layered structure.[55] Furthermore, according to the Rietveld refinement, the Li/Ni cation mixing were decreased from 3.28% for NMC to 2.95% for NMFAC with the addition of dual dopant Fe/Al (Fig. S1a,

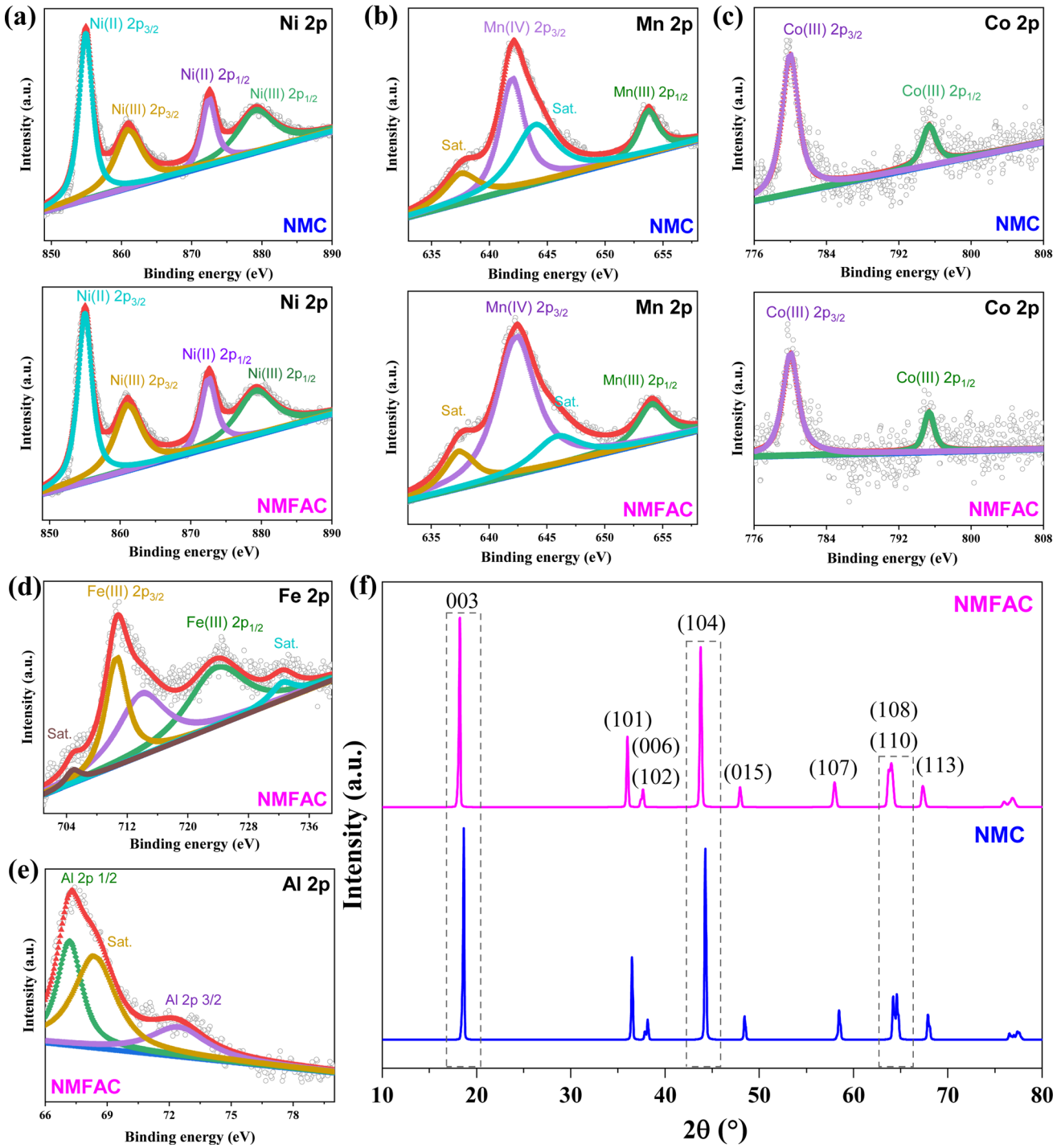

Fig. 3 XPS spectra for (a) Ni 2p, (b) Mn 2p, (c) Co 2p, (d) Fe 2p, and (e) Al 2p for NMC and NMFAC. (f) XRD patterns for NMC and NMFAC.

b and Table S1†). It can also be observed that the (003) and (104) peaks shift to lower angle with the addition of Fe/Al, indicating the larger value of c(Å)-axis, offers a larger channel for Li^+ diffusion, which is beneficial to the rate capability.[56] The atomic ratios of the hydroxide precursor and the two cathode samples are presented in the ICP-AES test results (Table S3†), indicating the successful synthesis of all components in accordance with stoichiometry.

The morphology and chemical compositions were examined using a SEM, TEM and EDX. The SEM images of $Ni_{0.90}Mn_{0.05}Fe_{0.02}Al_{0.02}Co_{0.01}(OH)_2$ and $Ni_{0.90}Mn_{0.05}Co_{0.05}(OH)_2$ hydroxides are shown in Fig. S2.† Overall, two hydroxides have similar particle sizes, but Fe/Al co-doping appears to have induced slight modifications in surface roughness, as evident by fine ridges on the surface of $Ni_{0.90}Mn_{0.05}Fe_{0.02}Al_{0.02}Co_{0.01}(OH)_2$. However, such a difference in surface roughness does not affect

the particle sizes and morphologies of the final NMC and NMFAC products as both exhibit similar particle sizes 2–4 μm with an octahedral shape (Fig. 4a and e). EDS mapping along with SEM imaging reveals that the Fe/Al is effectively doped with uniform distribution of Ni, Mn, Fe, Al, Co and O elements without changing morphology (Fig. 4d and h). Furthermore, the NMFAC bulk particle still has layered structure, as demonstrated by the TEM (Fig. 4b, c, f and g), identifying the (003) facet with a typical interplanar spacing of 0.48 nm. Consistent with the XRD conclusion and DFT calculations, the TEM analysis validates that the new cathode NMFAC displays a typical α-$NaFeO_2$ hexagonal layered structures with the $\bar{R}3m$ space group and high purity.

The electrochemical performances of NMC and NMFAC cathodes were initially evaluated in a coin half-cell configuration with a Li-metal anode at different current rate (where 1C = 200 mA g^{-1}) within a voltage range of 2.8–4.3 V. Fig. 5a shows the charge–discharge curves for NMC and NMFAC cathodes at 0.2C rate, demonstrating almost a similar specific discharge capacity of 217 and 220 mA h g^{-1}, respectively. However, the specific charge capacity is pretty higher for NMFAC (248 mA h g^{-1}) as compared to NMC (235 mA h g^{-1}). The dQ/dV curves in Fig. 5b shows that both NMC and NMFAC undergo a sequence of phase transitions starting from the initial hexagonal phase (H1) and progressing towards two additional hexagonal phases (H2 and H3), transitioning *via* a monoclinic phase (M) near 4 V.[57] The redox peaks in the dQ/dV curves of NMC and NMFAC around 4.2 V, linked to the H2–H3 phase transition, exhibit distinct differences. These peaks show a noticeable decrease in intensity and an increase in width upon the introduction of Fe/Al. A sharp redox peak during the H2–H3 transition typically indicates a sudden and detrimental structural change.[55] A well suppressed H2–H3 redox peaks in the dQ/dV curves for the NMFAC suggests that the Fe/Al co-dopant incorporated into the crystal structure protracts the detrimental phase transition. The rate capability comparison of NMC and NMFAC cathodes indicates that NMFAC consistently outperforms to its NMC counterpart, offering a maximum reversible discharge capacity of 221 mA h g^{-1} at a current rate of 0.2C (Fig. 5c). Moreover, the discharge capacity of NMC drops to 173 mA h g^{-1} at 3.0C, while NMFAC still delivers a discharge capacity of 176 mA h g^{-1}. Although both NMC and NMFAC cathodes exhibit a similar initial capacity, obvious difference occurs upon subsequent cycles. The cycling performance for

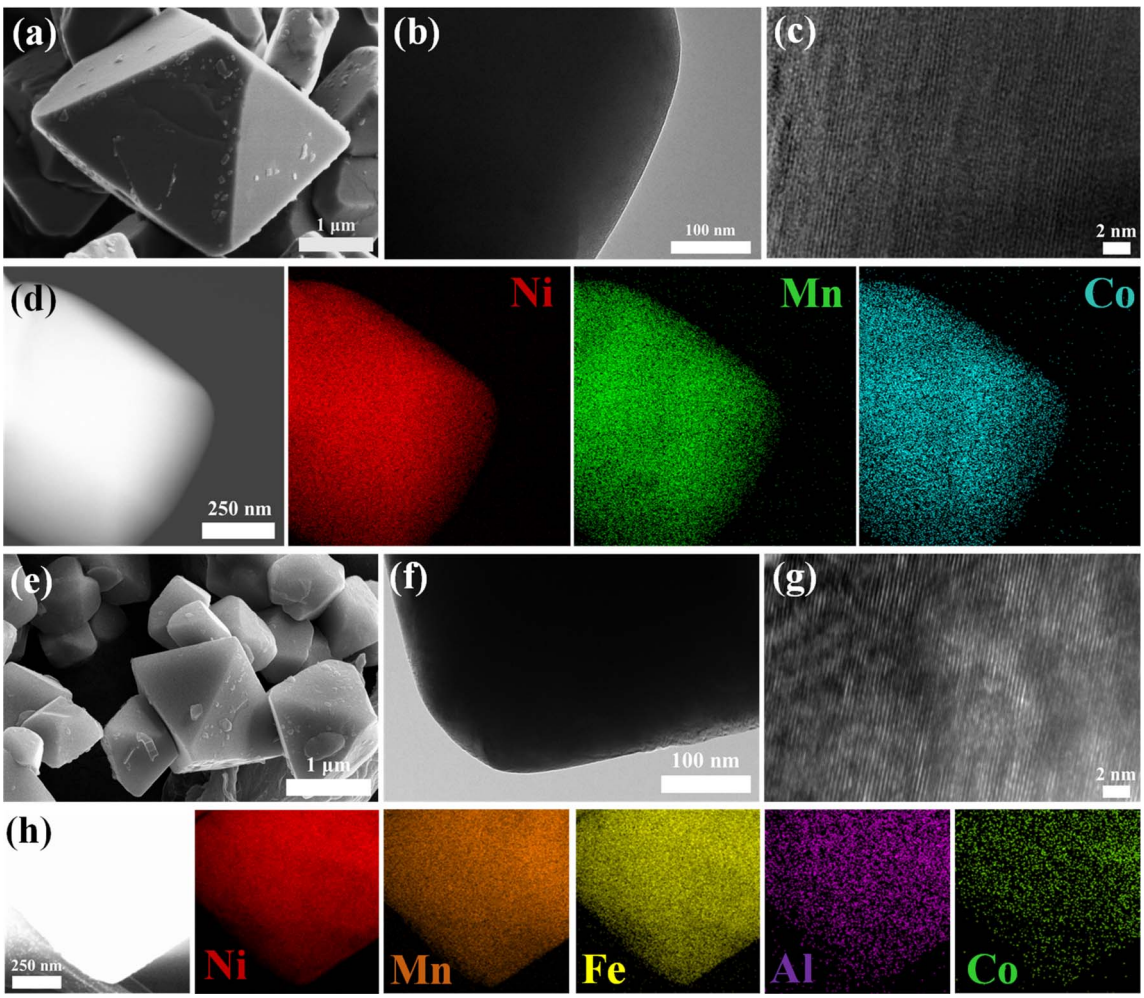

Fig. 4 SEM, TEM and EDS analysis of (a–d) NMC and (e–h) NMFAC.

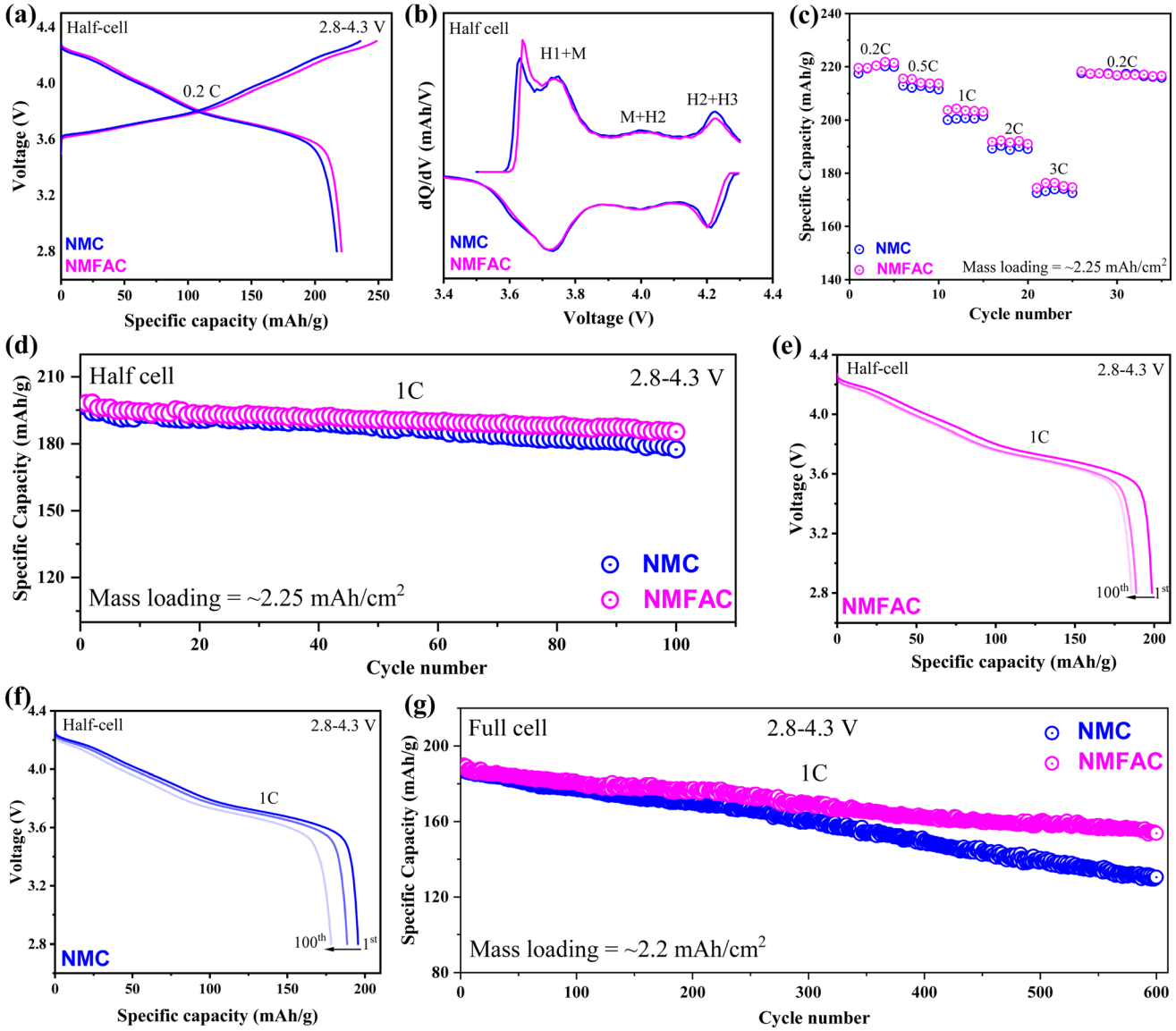

Fig. 5 (a) Charge–discharge capacity and (b) dQ/dV curves at 0.2C. (c) Rate performance with different current rate for NMC and NMFAC. (d) Cycle performance, (e and f) charge–discharge curves for coin half-cells with NMC and NMFAC cathodes. (g) Cycle performance for full-cells with NMC and NMFAC cathodes.

half cells at 1C rate reveal maximum capacities of 196 and 198 mA h g^{-1} for NMC and NMFAC cathodes, respectively (Fig. 5d). It is evident that NMFAC experiences lower capacity decay with 93% retention rate after 100 cycles. In contrast, the NMC cell displays higher capacity decay with 90% retention rate.

The long-term cycling performance of NMC and NMFAC cathodes for full-cell employing commercial graphite anodes are attempted to comprehensively evaluate their suitability for various industrial applications. The short cycle life observed in half-cells utilizing Li-metal anodes, compared to full-cells with graphite anodes, can be attributed primarily to issues such as dendritic formation and other related challenges during cycling, leading to the depletion of active-Li and electrolyte consumption. NCM and NMFAC delivered the highest discharge capacity of 186 and 189 mA h g^{-1}, respectively, at 1C for full-cell (Fig. 5g). After 600 cycles, both NCM and NMFAC exhibit a decline in discharge capacities to 129 and 154 mA h g^{-1}, respectively, with a capacity retention of 70% and 81% (Fig. 5g and S3†). These results reveal that the unique structure design of NMFAC can significantly enhance the cycle stability when compared with NMC (Fig. 5 and Table S5†). In addition, when compared with the previously reported Ni-rich cathodes, NMFAC also exhibits advantages. As shown in Table S6,† among all Ni-rich cathodes with 100 cycles only one cathode with Al/Mg co-doping processes the same capacity retention (93%) as NMFAC, but it contains higher Co concentration (0.042 moles) than NMFAC (only 0.01 moles). When the initial charge capacity of NMFAC is compared with that of the previously reported co-doped Ni-rich cathodes (Table S7†),

NMFAC also has advantages by delivering 248 mA h g^{-1} at 0.2C rate while all other studies have lower specific capacities even at 0.1C rate with only one exception which delivers 252 mA h g^{-1} specific capacity.

To provide more insights into the mechanism(s) through which NMFAC delivers better electrochemical properties than NMC, EIS analysis was conducted (Fig. S4†). The EIS curves of both NMC and NMFAC cells before cycling consist of a depressed semicircle and a sloped line (Fig. S4a†) and can be fitted with an equivalent circuit, $R_s(Q_{ct}R_{ct})W$. The semicircle ($Q_{ct}R_{ct}$) is regarded as the charge transfer resistance and the sloped line is related to the Warburg impedance (W), while the intercept with real axis (Z') at the highest frequency range is assigned to the solution resistance (R_s). After 100 cycles the EIS curves of both materials exhibit three depressed semicircles (Fig.s S4b†) and can be fitted with an equivalent circuit of $R_s(Q_{SEI}R_{SEI})(Q_{int}R_{int})(Q_{ct}R_{ct})W$. Here ($Q_{SEI}R_{SEI}$) appearing at the high frequency range is due to the resistance of the solid electrolyte interface (SEI) film formed on the electrode during high-voltage cycling, whereas ($Q_{int}R_{int}$) emerged with the ($Q_{SEI}R_{SEI}$) semicircle but at the slightly lower frequency is attributed to interphase contact resistance. R_s, ($Q_{ct}R_{ct}$) and W have the same meanings as those before cycling. As summarized in Table S4,† the charge transfer resistance has increased dramatically for both NMC and NMFAC cells after 100 cycles, but the final charge transfer resistance of the NMFAC cell is smaller (431 Ω) than that of the NMC cell (495 Ω). Furthermore, the NMFAC cell also has smaller values for all other resistances, R_s, R_{SEI}, and R_{int}, when compared with the NMC cell after 100 cycles, revealing that the NMFAC cell has a smaller increase in the internal resistance of the cell and thus has better cycle stability and rate capability.

The primary challenges associated with high Ni-rich cathode materials involve surface and structural deteriorations during long term cycling. Thus, to further understand the mechanism(s) through which NMFAC exhibits better electrochemical properties than NMC, high mass and spatial resolutions of TOF-SIMS chemical imaging were used to observe the surface chemistry and CEI of NMC and NMFAC cathode materials after cycling (Fig. 6a). The TOF-SIMS mappings of various fragments of interest from the cycled NMC and NMFAC cathode particles reveal that the interaction between the cathode particles and F-containing species in the electrolyte, such as PF_6 and its hydrolysis products POF_2 and HF, led to the generation of LiF_2 and the fluorinated TM fragment NiF_3.[46,58] However, the NiF_3 and LiF_2 contents were higher in NMC as compared to NMFAC, suggesting more adverse cathode–electrolyte reactions occur on the surface of NMC than on the surface of NMFAC. Additionally, the degraded interphase on NMC extends deeper inside the cathode, as evidenced by overlay mapping results of NiO_2 fragments, C_2HO fragments, and PO_2 fragments in NMC and NMFAC. Overall, the TOF-SIMS mapping results indicate that NMFAC can better withstand electrolyte attacks compared to NMC cathode. Furthermore, analysis of recovered cathode electrodes reveals the total integrated yields of each fragment, including $LiPF_6$ breakdown fragments (PO_2/POF_3), organic solvent decomposition fragments ($LiO_2/C_2HO/C_2H_3O$), and active material dissolution fragments (LiF_3/F_2) (Fig. 6b). It is interesting that most of the fragment counts between NMC and NMFAC cathodes are not significantly different. A few higher fragment counts ($LiO_2/POF_3/C_3F$) in NMFAC indicates that the electrode–electrolyte reaction products based on fragments are more concentrated near the surface of NMFAC, possibly preventing electrolyte reactions from penetrating deeper into the bulk material. Compared to NMFAC, which appears to be less reactive during usage, the intensity of C_2HO/C_2H_3O fragments indicates that NMC is significantly more susceptible to detrimental EC-based electrolyte oxidation processes during prolonged cycling. Similarly, the LiF_2/F_2 data suggests that the active material dissolution reaction, mainly triggered by $LiPF_6$ hydrolysis processes, is much more severe for NMC than for NMFAC.

SEM images reveal that the inner main particles of NMFAC display smoother surfaces than those of NMC (Fig. S5†). This suggests significant structural degradation in the original NMC cathode, possibly induced by inner anisotropic strain during deep cycling. Conversely, due to the distinctive integrated structure of SC primary particles, SEM images indicate that both electrodes maintained mechanical integrity without visible cracks even after 600 cycles, preserving their morphology well. Moreover, TEM images illustrate the visibility of the $Fm\bar{3}m$ rock-salt phase from the exterior to the interior of the main particle, suggesting severe corrosion resulting from unfavorable electrode/electrolyte interphase side reactions (Fig. S5†). The existence of a small layer of CEI on the surface of the NMFAC electrode provides stronger evidence of the structural integrity of SC particles without electrolyte penetration compared to NMC. Unlike the cycled electrode, where the disordered rock-salt NiO phase occurs, the $\bar{R}3m$ layered structure remains well-maintained without experiencing irreversible alteration. The structural integrity of the micron-sized particle is preserved to a high degree. According to the outcome, Fe/Al co-doping can provide a stable CEI, which can significantly reduce the likelihood of adverse reactions and stabilize structural alterations.

Furthermore, during extended cycling only a thin layer of the disordered phase remains on the surface of the bulk structure, maintaining the original $\bar{R}3m$ layered structure. The substantial volume change experienced by primary particles in the NMC cathode induces significant microstrains over prolonged cycling periods, as illustrated by the schematic diagram depicting internal structure progression. This phenomenon can result in the formation of a thick CEI layer, facilitating the generation of microcracks and eventual disintegration of primary particles (Fig. 7). An irreversible phase transition from an ordered layered structure to a disordered spinel/rock salt phase, which spreads from the surface into the inner bulk, typically impacts pristine NMC. This transformation is characterized by anisotropic volume changes accompanied by localized stress shrinkage. This will impede the diffusion of Li-ions and accelerate the deterioration of capacity. Furthermore, the recurrent cycling induces nanoscale intergranular cracks that enhance the electrolyte's penetration into the SC architecture. This can lead to severe reactions at the electrode/electrolyte interface and worsen the collapse of the structure. Moreover, electrolyte

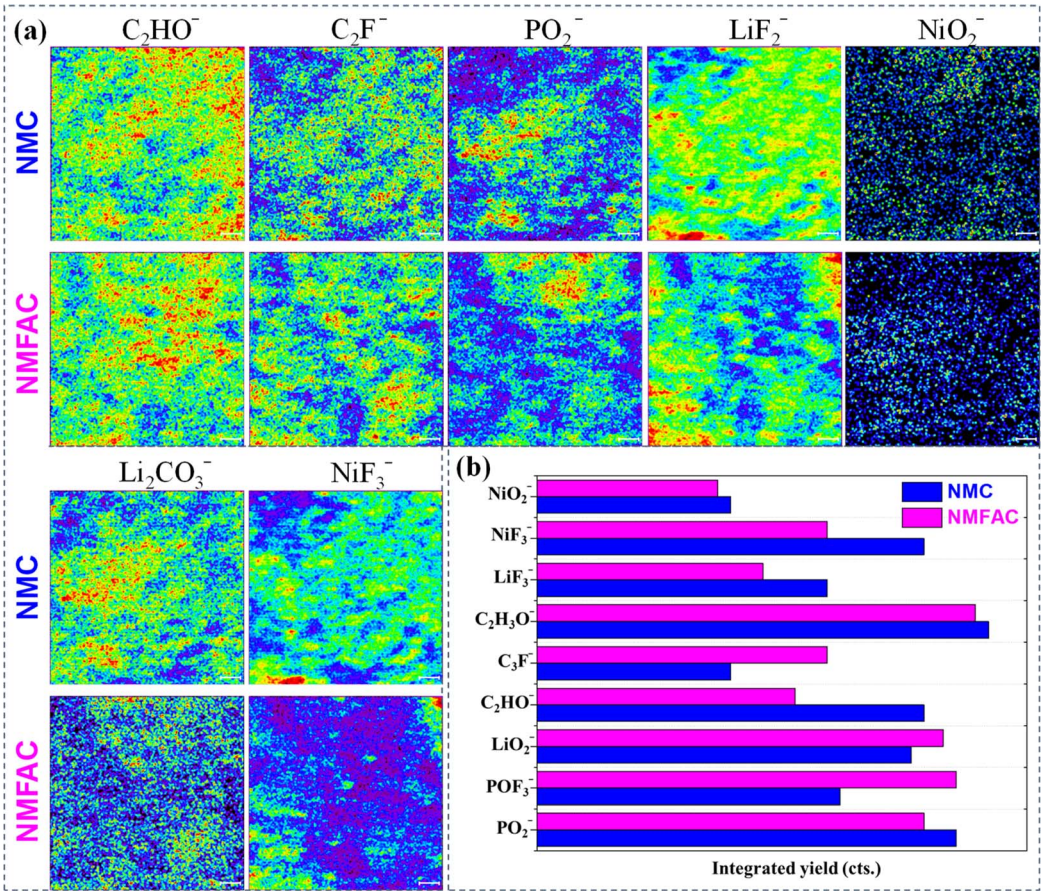

Fig. 6 (a) TOF-SIMS chemical imaging and (b) integrated yields of the secondary-ion fragments of cathodes after 600 cycles.

infiltration triggering irreversible phase transitions exacerbates the structural degradation of the newly exposed cathode surface. The densely disordered structure impedes Li^+ diffusion, accelerating capacity degradation and shortening cycle life. Conversely, the NMFAC cathode, owing to Fe/Al addition embedded within its underlying structure, exhibits anisotropic microstrains, inherently resisting microcrack formation. The even distribution of Fe/Al, offering both bulk and surface stability, notably curbs the continuous expansion of undesirable rock-salt phase and CEI layers induced by electrolyte erosion. Furthermore, Fe/Al diminishes Li/Ni cation mixing and truncates Li^+ diffusion pathways, enhancing the long-term cycle

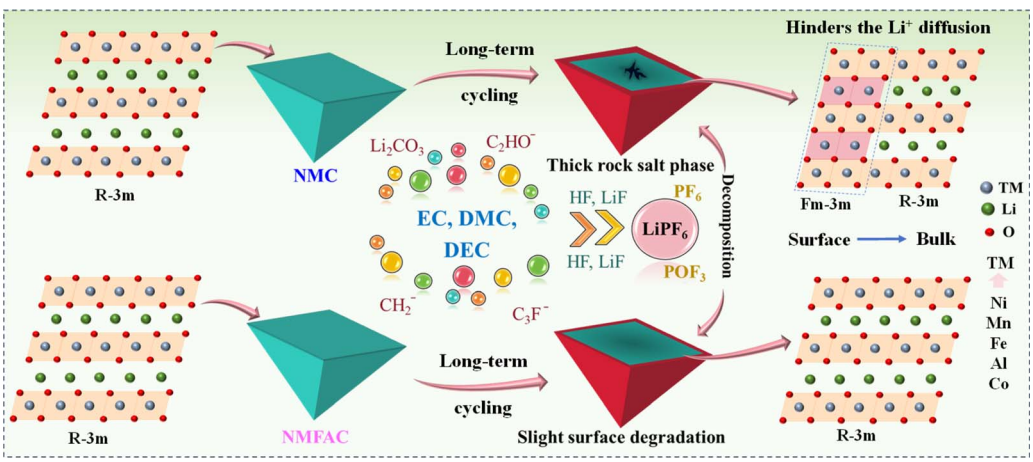

Fig. 7 Schematic illustration of crack evolution and the internal morphological difference for NMC and NMFAC cathodes after long-term cycling.

stability of LIBs. More significantly, Fe/Al and oxygen together fill the tetrahedral gap of oxygen caused by Fe/Al-occupation on the transition metal (TM) site. This can greatly increase the layered distance and enhance the thermodynamics and kinetics of the Ni-rich electrode, guaranteeing the superior rate capability.

4. Conclusion

In summary, the dynamic stability of Fe/Al co-doped SC low-Co Ni-rich cathode materials holds great promise for advancing the performance and reliability of LIBs. The as-prepared NMFAC cathode has made a significant progress in achieving dynamic stability by utilizing a combination of straightforward synthesis techniques, thorough characterization, and computational modeling. The cycle performance of NMFAC cathode has been greatly enhanced even at high current rates. NMFAC delivers a high specific discharge capacity of 221 mA h g^{-1} at 0.2C and a stable cycling performance with a 93% retention for 100 cycles at 1C. In particular, for full cells, it exhibits a high-capacity retention of 81% over 600 cycles and a higher reversible capacity of 154 mA h g^{-1}. This work highlights the potential of the Fe/Al co-doping strategy as a viable route towards realizing high-performance and long-lasting LIB systems, addressing the critical challenges in energy storage technology. Continued efforts in this field are essential for realizing the full potential of Ni-rich cathodes and accelerating the adoption of high-performance LIBs in various applications.

Data availability

Data will be made available on reasonable request.

Conflicts of interest

The authors declare that they have no known competing financial interests or personal relationships that could have appeared to influence the work reported in this paper.

Acknowledgements

This research was financially supported by the U.S. National Science Foundation (NSF) with the award numbers OISE-2230770. Leon Shaw is also grateful to the Rowe Family Endowment Fund. Rashid Iqbal thanks to National Science Foundation of China (22350410376).

References

1 Y. Ding, Z. P. Cano, A. Yu, J. Lu and Z. Chen, *Electrochem. Energy Rev.*, 2019, **2**, 1–28.
2 J. Duan, X. Tang, H. Dai, Y. Yang, W. Wu, X. Wei and Y. Huang, *Electrochem. Energy Rev.*, 2020, **3**, 1–42.
3 A. Saleem, R. Iqbal, M. K. Majeed, A. Hussain, A. R. Akbar, Z. Hussain, B. Jabar, S. Rauf and L. L. Shaw, *Nano Energy*, 2024, **128**, 109848.
4 H. Zhou, F. Xin, B. Pei and M. S. Whittingham, *ACS Energy Lett.*, 2019, **4**, 1902–1906.
5 M. Aizudin, W. Fu, R. P. Pottammel, Z. Dai, H. Wang, X. Rui, J. Zhu, C. C. Li, X.-L. Wu and E. H. Ang, *Small*, 2024, **20**, 2305217.
6 K. Chen, P. Barai, O. Kahvecioglu, L. Wu, K. Z. Pupek, M. Ge, L. Ma, S. N. Ehrlich, H. Zhong, Y. Zhu, V. Srinivasan, J. Bai and F. Wang, *Nat. Commun.*, 2024, **15**, 430.
7 N. Muralidharan, E. C. Self, M. Dixit, Z. Du, R. Essehli, R. Amin, J. Nanda and I. Belharouak, *Adv. Energy Mater.*, 2022, **12**, 2103050.
8 Y.-K. Sun, *ACS Energy Lett.*, 2022, **7**, 1774–1775.
9 J. U. Choi, N. Voronina, Y.-K. Sun and S.-T. Myung, *Adv. Energy Mater.*, 2020, **10**, 2002027.
10 A. Saleem, L. L. Shaw, R. Iqbal, A. Hussain, A. R. Akbar, B. Jabar, S. Rauf and M. K. Majeed, *Energy Storage Mater.*, 2024, **69**, 103440.
11 J. Liu, J. Wang, Y. Ni, K. Zhang, F. Cheng and J. Chen, *Mater. Today*, 2021, **43**, 132–165.
12 M. Li and J. Lu, *Science*, 2020, **367**, 979–980.
13 Y. Xiao, T. Liu, J. Liu, L. He, J. Chen, J. Zhang, P. Luo, H. Lu, R. Wang and W. Zhu, *Nano Energy*, 2018, **49**, 77–85.
14 L. Ni, R. Guo, S. Fang, J. Chen, J. Gao, Y. Mei, S. Zhang, W. Deng, G. Zou and H. Hou, *EScience*, 2022, **2**, 116–124.
15 F. Kong, C. Liang, L. Wang, Y. Zheng, S. Perananthan, R. C. Longo, J. P. Ferraris, M. Kim and K. Cho, *Adv. Energy Mater.*, 2019, **9**, 1802586.
16 G.-T. Park, B. Namkoong, S.-B. Kim, J. Liu, C. S. Yoon and Y.-K. Sun, *Nat. Energy*, 2022, **7**, 946–954.
17 R. Zhang, C. Wang, P. Zou, R. Lin, L. Ma, L. Yin, T. Li, W. Xu, H. Jia and Q. Li, *Nature*, 2022, **610**, 67–73.
18 D. Rathore, M. Garayt, Y. Liu, C. Geng, M. Johnson, J. Dahn and C. Yang, *ACS Energy Lett.*, 2022, **7**, 2189–2195.
19 X. Yao, X. Song, F. Zhang, J. Ma, H. Jiang, L. Wang, Y. Liu, E. Huixiang Ang and H. Xiang, *ChemElectroChem*, 2022, **9**, e202200390.
20 Q. Chang, Y. X. Angel Ng, D. Yang, J. Chen, T. Liang, S. Chen, X. Zhang, Z. Ou, J. Kim, E. H. Ang, H. Xiang and X. Song, *ACS Mater. Lett.*, 2023, **5**, 1506–1526.
21 X. Song, X. Yao, F. Zhang, E. H. Ang, S. Rong, K. Zhao, K. He and H. Xiang, *J. Membr. Sci.*, 2023, **685**, 121951.
22 J. Shen, B. Zhang, W. Huang, X. Li, Z. Xiao, J. Wang, T. Zhou, J. Wen, T. Liu, K. Amine and X. Ou, *Adv. Funct. Mater.*, 2023, **33**, 2300081.
23 X. Ou, T. Liu, W. Zhong, X. Fan, X. Guo, X. Huang, L. Cao, J. Hu, B. Zhang, Y. S. Chu, G. Hu, Z. Lin, M. Dahbi, J. Alami, K. Amine, C. Yang and J. Lu, *Nat. Commun.*, 2022, **13**, 2319.
24 A. Saleem, A. Hussain, M. Z. Ashfaq, M. S. Javed, S. Rauf, M. M. Hussain, A. Saad, J. Shen, M. K. Majeed and R. Iqbal, *J. Alloys Compd.*, 2022, **924**, 166375.
25 A. Saleem, M. K. Majeed, R. Iqbal, A. Hussain, M. S. Naeem, S. Rauf, Y. Wang, M. S. Javed and J. Shen, *Adv. Mater. Interfaces*, 2022, **9**, 2200800.
26 G. Liu, M. Li, N. Wu, L. Cui, X. Huang, X. Liu, Y. Zhao, H. Chen, W. Yuan and Y. Bai, *J. Electrochem. Soc.*, 2018, **165**, A3040.

27 J. Sun, X. Cao, H. Yang, P. He, M. A. Dato, J. Cabana and H. Zhou, *Angew. Chem., Int. Ed.*, 2022, **61**, e202207225.
28 T. Liu, L. Yu, J. Liu, J. Lu, X. Bi, A. Dai, M. Li, M. Li, Z. Hu and L. Ma, *Nat. Energy*, 2021, **6**, 277–286.
29 W. Li, S. Lee and A. Manthiram, *Adv. Mater.*, 2020, **32**, 2002718.
30 Z. Cui, Q. Xie and A. Manthiram, *Adv. Energy Mater.*, 2021, **11**, 2102421.
31 D. Goonetilleke, A. Mazilkin, D. Weber, Y. Ma, F. Fauth, J. Janek, T. Brezesinski and M. Bianchini, *J. Mater. Chem. A*, 2022, **10**, 7841–7855.
32 W. Yan, S. Yang, Y. Huang, Y. Yang and Y. Guohui, *J. Alloys Compd.*, 2020, **819**, 153048.
33 J. Wu, J. Yang, J. Zheng, M. Wang, S. Li, B. Huang, Y. Li, Q. Zhu, Q. Chen, S. Xiao and B. Liu, *ChemSusChem*, 2023, **16**, e202300607.
34 S.-B. Lee, N.-Y. Park, G.-T. Park, U.-H. Kim, S.-J. Sohn, M.-S. Kang, R. M. Ribas, R. S. Monteiro and Y.-K. Sun, *ACS Energy Lett.*, 2024, **9**, 740–747.
35 N.-Y. Park, G. Cho, S.-B. Kim and Y.-K. Sun, *Adv. Energy Mater.*, 2023, **13**, 2204291.
36 N.-Y. Park, S.-B. Kim, M.-C. Kim, S.-M. Han, D.-H. Kim, M.-S. Kim and Y.-K. Sun, *Adv. Energy Mater.*, 2023, **13**, 2301530.
37 D. L. Wood, M. Wood, J. Li, Z. Du, R. E. Ruther, K. A. Hays, N. Muralidharan, L. Geng, C. Mao and I. Belharouak, *Energy Storage Mater.*, 2020, **29**, 254–265.
38 T. Ohzuku, A. Ueda and M. Nagayama, *J. Electrochem. Soc.*, 1993, **140**, 1862.
39 R. D. Shannon, *Acta Crystallogr. A*, 1976, **32**, 751–767.
40 J. Kim, H. Lee, H. Cha, M. Yoon, M. Park and J. Cho, *Adv. Energy Mater.*, 2018, **8**, 1702028.
41 W. Li, E. M. Erickson and A. Manthiram, *Nat. Energy*, 2020, **5**, 26–34.
42 W. Li, X. Liu, H. Celio, P. Smith, A. Dolocan, M. Chi and A. Manthiram, *Adv. Energy Mater.*, 2018, **8**, 1703154.
43 T. Ohzuku and Y. Makimura, *Chem. Lett.*, 2001, **30**, 642–643.
44 C. Chen, J. Liu, M. Stoll, G. Henriksen, D. Vissers and K. Amine, *J. Power Sources*, 2004, **128**, 278–285.
45 J. Zheng, Y. Ye, T. Liu, Y. Xiao, C. Wang, F. Wang and F. Pan, *Acc. Chem. Res.*, 2019, **52**, 2201–2209.
46 A. Saleem, H. Zhu, M. K. Majeed, R. Iqbal, B. Jabar, A. Hussain, M. Z. Ashfaq, M. Ahmad, S. Rauf, J. P. Mwizerwa, J. Shen and Q. Liu, *ACS Appl. Mater. Interfaces*, 2023, **15**, 20843–20853.
47 Q. He, B. Yu, Z. Li and Y. Zhao, *Energy Environ. Mater.*, 2019, **2**, 264–279.
48 G. Zha, W. Hu, S. Agarwal, C. Ouyang, N. Hu and H. Hou, *Chem. Eng. J.*, 2021, **409**, 128343.
49 H. Yu, Y. Cao, L. Chen, Y. Hu, X. Duan, S. Dai, C. Li and H. Jiang, *Nat. Commun.*, 2021, **12**, 4564.
50 Q. Xu, X. Li, H. M. Kheimeh Sari, W. Li, W. Liu, Y. Hao, J. Qin, B. Cao, W. Xiao, Y. Xu, Y. Wei, L. Kou, Z. Tian, L. Shao, C. Zhang and X. Sun, *Nano Energy*, 2020, **77**, 105034.
51 W. Liu, X. Li, Y. Hao, D. Xiong, H. Shan, J. Wang, W. Xiao, H. Yang, H. Yang, L. Kou, Z. Tian, L. Shao and C. Zhang, *Adv. Funct. Mater.*, 2021, **31**, 2008301.
52 C.-a. Lin, R. N. Nasara and S.-k. Lin, *ACS Sustain. Chem. Eng.*, 2021, **9**, 11342–11350.
53 H. Li, M. Cormier, N. Zhang, J. Inglis, J. Li and J. R. Dahn, *J. Electrochem. Soc.*, 2019, **166**, A429.
54 J. Zheng, G. Teng, C. Xin, Z. Zhuo, J. Liu, Q. Li, Z. Hu, M. Xu, S. Yan, W. Yang and F. Pan, *J. Phys. Chem. Lett.*, 2017, **8**, 5537–5542.
55 H.-H. Ryu, B. Namkoong, J.-H. Kim, I. Belharouak, C. S. Yoon and Y.-K. Sun, *ACS Energy Lett.*, 2021, **6**, 2726–2734.
56 X. Ma, P. Vanaphuti, J. Fu, J. Hou, Y. Liu, R. Zhang, S. Bong, Z. Yao, Z. Yang and Y. Wang, *Nano Energy*, 2021, **87**, 106194.
57 H.-H. Ryu, K.-J. Park, C. S. Yoon and Y.-K. Sun, *Chem. Mater.*, 2018, **30**, 1155–1163.
58 Y. Chen, W. Zhao, Q. Zhang, G. Yang, J. Zheng, W. Tang, Q. Xu, C. Lai, J. Yang and C. Peng, *Adv. Funct. Mater.*, 2020, **30**, 2000396.